Meteorol Atmos Phys 88, 1–21 (2005)
DOI 10.1007/s00703-003-0047-6

Meteorology
and Atmospheric
Physics

Printed in Austria

[1] Department of Land, Air, and Water Resources, University of California, Davis, CA, USA
[2] Department of Marine, Earth, and Atmospheric Sciences, North Carolina State University, Raleigh, NC, USA

Orographic effects on a conditionally unstable flow over an idealized three-dimensional mesoscale mountain

S.-H. Chen[1] and **Y.-L. Lin**[2]

With 15 Figures

Received April 1, 2003; revised May 26, 2003; accepted June 30, 2003

Summary

Idealized numerical simulations using the Weather and Research Forecast (WRF) model indicate that three flow regimes, based on the moist Froude number, can be identified for a conditionally unstable, rotational, horizontally homogeneous, uniformly stratified flow over an idealized, three-dimensional, mesoscale mountain stretched spanwise to the impinging flow: (I) a quasi-stationary upslope convective system and an upstream-propagating convective system, (II) a quasi-stationary upslope convective system, and (III) a stationary upslope convective system and a quasi-stationary downstream convective system. Several major differences from a similar type of flow with no rotation over a two-dimensional mountain range are found. One important finding is that relatively strong mean flow produces a quasi-stationary mesoscale convective system (MCS) and maximum rainfall on the windward slope (upslope rain), instead of on the mountain peak or over the lee side.

We found that the Coriolis force helps produce heavy upslope rainfall by making transition from "flow-around" the eastern part of the upslope to "flow-over" the western part of the upslope (transits to a higher flow regime) by deflecting the incident southerly flow to become east–south-easterly barrier winds. We found that the addition of the western flank of the arc-shaped mountain helps slow down the barrier wind from east and causes the maximum rainfall to move east of the windward slope. A lower-Froude number flow tends to produce a rainfall maximum near the concave region.

Several other important facts can also be found in this study. The ratio of the maximum grid scale rainfall to the sub-grid scale rainfall increases when the moist Froude number increases. When the CAPE decreases, it is found that the upstream moist flow tends to shift to a higher Froude-number regime. Therefore, the Froude number cannot solely be used to define a moist flow regime when different CAPEs are considered. In another word, other parameters, such as CAPE, might play an important role in determining moist flow regimes.

1. Introduction

Heavy orographic rainfall may occur on the windward slope, upstream of the plain area, or over the lee slope of a mesoscale mountain range (Smith, 1979; Banta, 1990; Houze, 1993; Lin, 1993). Based on idealized numerical experiments of two-dimensional (2D), nonrotating, conditionally unstable airflow over a mesoscale mountain range, Chu and Lin (2000) identified three moist flow regimes: (I) upstream propagating convective systems, (II) quasi-stationary convective systems, and (III) both quasi-stationary and downstream propagating convective systems. These flow regimes are controlled by the moist Froude number, which is defined as $F_w = U/N_w h$, where U is the incoming (uniform) flow speed, $N_w (= g/\theta_v \cdot \partial\theta_v/\partial z)$ is the moist Brunt-Vaisala or buoyancy frequency, h the maximum mountain height and θ_v the virtual potential temperature.

For a dry atmosphere, the air flow can transit from a "*flow-over*" to a "*flow-around*" regime when the nondimensional mountain height ($\tilde{h} = Nh/U$, i.e., the inverse Froude number) increases above a critical value, such as 1.2 for an axisymmetric Gaussian mountain and a non-rotational flow (Smith and Gronas, 1993; Smolarkiewicz and Rotunno, 1989), and flow regimes can be modified by the obstacle shape (i.e., the aspect ratio; Bauer et al, 2000). Using a stratified sounding, Miglietta and Buzzi (2001) studied the role of moisture in the change of flow regimes (flow over or flow around) over a mesoscale circular obstacle without the Earth's rotation effect. They examined various nondimensional mountain heights and claimed that with intermediate obstacle heights the humidity that could change the precipitation amount and the flow regime to a lower Froude number is very important to the flow behavior.

Based on the arguments in Lin et al (2001), a low-level jet (LLJ) is one of the common ingredients necessary for heavy orographic rainfall. Due to the existence of a high wind speed, the moist Froude number (F_w) will have a relatively high value since U is large in this case. Therefore, instead of using different mountain heights (Miglietta and Buzzi, 2001; Olafsson and Bougeault, 1997; Thorsteinsson and Sigurdsson, 1996), here we are interested in applying a variety of basic flows to understand the impact of the moist Froude number on the propagation of three-dimensional (3-D) orographically-induced convective systems.

In addition to F_w, the location of the heavy orographic rainfall is also strongly influenced by the geometry of obstacles (Schneidereit and Schär, 2000) and the Earth's rotation through the presence of the Coriolis force (Trub and Davies, 1995; Thorsteinsson and Sigurdsson, 1996; Olafsson and Bougeault, 1997) when mesoscale mountains are considered. Many heavy orographic rainfall events occur in the Alps near the Lago Maggiore, Ticino, and Piedmont regions, in proximity to the concave region of mountain ranges (Binder and Schär, 1996; Buzzi and Foschini, 2000). Similar phenomena also occur in heavy orographic rainfall events in Taiwan, where the island's Central Mountain Range (CMR) is oriented in a north–northeast to south–southwest direction. Under the influence of a southwesterly monsoon, heavy orographic rainfall events often start near a concave region of the CMR in the southwest of Taiwan (Lin et al, 2001; Chiao and Lin, 2003).

Schneidereit and Schär (2000) showed that if an east–west-oriented mountain barrier has a western flank, the flow in the presence of a southerly LLJ, which has a finite width, can undergo transitions from a regime of "go-around" to "go-over" the mountain. However, they did indicate that the region of maximum rainfall is sensitive to the location of the finite-width LLJ. Besides the influence of the arc-shaped mountain, in studying the 1994 Piedmont flood, Rotunno and Ferretti (2001) found that there was a strong horizontal moisture gradient upstream of the Alps; thus the western part of the moist airstream flowed over, while the drier eastern part was deflected westward around the obstacle, producing convergence between the two airstreams at the western side of the east–west main ridge.

For a low-level southerly flow of $15\,ms^{-1}$, which is used in our control run and is typical for the Alpine heavy orographic rainfall events, a $10^{-4}\,s^{-1}$ Coriolis parameter and a 200 km (L) horizontal mountain scale give a Rossby number ($R_o = U/fL$) of 0.75. Therefore, the Coriolis force should be taken into account in this situation. Due to the Earth's rotational effect, the flow regime can be shifted to a regime associated with a higher Froude number; in addition, the pressure drag is increased when the nondimensional height increases (Olafsson and Bougeault, 1997). Schneidereit and Schär (2000) found that the pronounced east–west asymmetry associated with the southerly flow is primarily induced by the Coriolis effect in the presence of an elongated mountain (which could be further intensified by an impinging LLJ as well as the arc-shaped Alpine geometry). Stein (2001) proposed that the easterly "barrier wind" (e.g., see Pierrehumbert and Wyman, 1985) south of the Alps is induced by the Coriolis force; this barrier wind then meets the impinging southerly flow, which flows along the western flank of the arc-shaped Alps, resulting in mesoscale convergence in the concave region.

In this study, we will investigate the formation of the upstream convergence, which is ultimately responsible for the triggering and initiation of orographically induced mesoscale convective systems in the concave region of the simplified Alps. In order to understand the dynamics, we will assume simple ambient environments with implications for possible explanations accompanying moist flow regime transitions. Beside those parameters mentioned above (i.e., the moist Froude number, the geometry of the mountain, and the Coriolis force), the effects of the convective available potential energy (CAPE) on the flow regime classification are also examined.

The paper is organized as follows. The numerical model description and experimental design will be presented in Sect. 2. Results, which are discussed in Sect. 3, include the three-dimensional (3D) moist flow regimes and the effects of the Earth rotation, mountain geometry, and Coriolis force. Concluding remarks appear in Sect. 4.

2. Model description and experiment design

The Weather Research and Forecast (WRF) model is a next-generation mesoscale model, developed by a group of scientists from different institutions and research centers (Chen and Dudhia, 2000; Michalakes et al, 2001; Skamarock et al, 2001). WRF is a fully compressible, three-dimensional (3D) nonhydrostatic model and the governing equations are written in flux-form. This model adopts the Arakawa-C grid and a time splitting explicit scheme (Klemp and Wilhelmson, 1978), and also has an option for a free-slip lower boundary condition, used for performing idealized simulations. Currently, two different prototypes of the WRF model are available (height coordinate and mass coordinate). The terrain-following height coordinate ($\sigma - z$) is used for our study. We also use the Runge-Kutta third-order time scheme, third-order advection schemes in both the horizontal and vertical directions, an open lateral boundary condition in the north–south direction, and a symmetric boundary condition with a zero normal wind to maintain the geostrophic balance of the basic wind in the east–west boundary. A free-slip lower boundary condition is used. Both the Kain–Fritsch (Kain and Fritsch, 1993) cumulus parameterization and Purdue Lin microphysics parameterization (Chen and Sun, 2002) schemes are activated in all the simulations. The Purdue Lin microphysics scheme is based on Lin et al (1983), and Rutledge and Hobbs (1984) with some modifications. Detailed information about the model may be found at: *www.wrf-model.org.*

The horizontally homogeneous initial conditions are specified using a simple analytical function. The surface potential temperature is 300 K, and the constant dry Brunt-Vaisala frequency is $0.0123\,s^{-1}$. The relative humidity decreases from 93% at the sea level to 25% at the height of

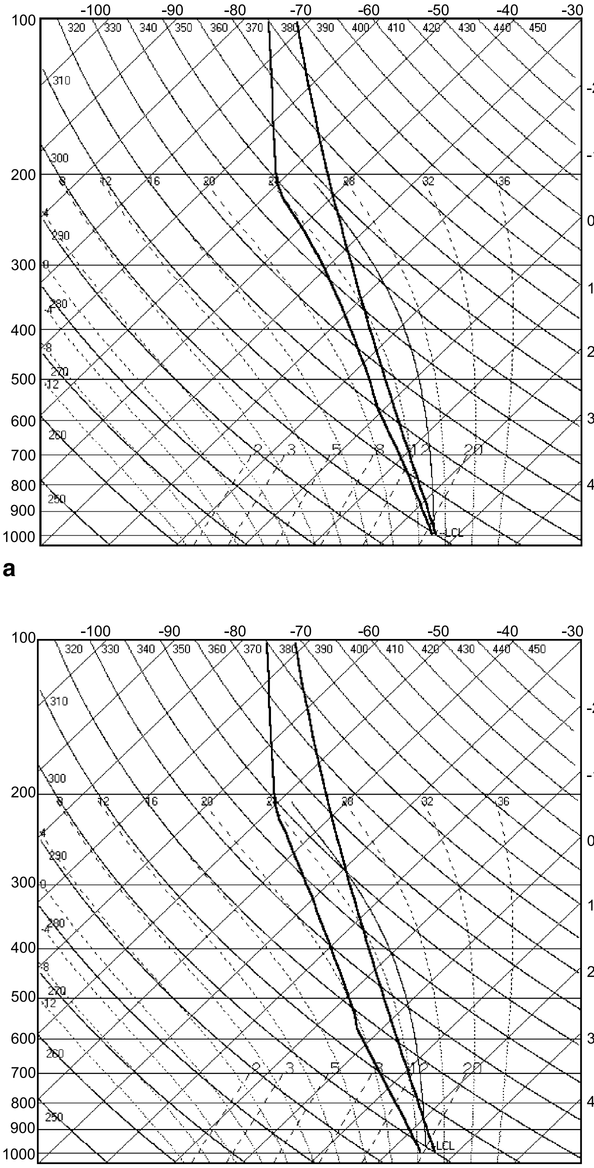

Fig. 1. Skew-T log-P diagrams of the idealized initial soundings used in the simulations. The CAPE associated with the sounding in (**a**) is approximately $2000\,J\,kg^{-1}$, and with the sounding in (**b**) is approximately $1000\,J\,kg^{-1}$

12 km, above which it remains constant at 25% to the model top of 24 km (Fig. 1a). The *moist Brunt-Vaisala frequency* (N_w) is approximately $0.01127\,s^{-1}$, which is roughly estimated from the surface to 1,500 m in a column away from the mountain ridge based on the following formula (Emanuel, 1994)

$$N_w^2 = \frac{g}{\theta_v}\frac{\partial \theta_v}{\partial z}, \tag{1}$$

where θ_v is the virtual potential temperature. A uniform southerly flow is imposed across the entire model domain, but is varied case by case in order to obtain different moist Froude numbers ($F_w = U/N_w h$ *see Table 1 for details*). The analytic initial conditions satisfy both hydrostatic and geostrophic balances. With these assumptions, the relationship among the potential temperature (θ), the dry Brunt-Vaisala frequency (N), and the horizontal wind velocity southerly: represented by (U) can be expressed as

$$\frac{\partial \ln \theta}{\partial x} = -\frac{N^2 f}{g^2}U, \tag{2}$$

where g is the gravitational acceleration and $f(= 1 \times 10^{-4}\,s^{-1})$ is the (constant) Coriolis parameter.

In this study, we use two types of idealized mountain geometries to represent the Alps, namely a ridge-like and arc-shaped orography, identical to those used by Schneidereit and Schär (2000). The ridge topography has an east–west length of 700 km and a north–south width of 400 km, whose maximum height decreases from the ridgeline to the foothills based on the $\cos^2$ function. The parameters for the mountain height (h), half-width (a), and grid spacing ($\Delta x = \Delta y$) in the x- and y-directions are $2\,km$, $100\,km$, and $30\,km$, respectively. The horizontal domain is partitioned by 111×111 grid points in the xy-directions, and covers an area of $3{,}300 \times 3{,}300\,km^2$. The vertical grid interval is stretched from about $30\,m$ at the lowest level to $500\,m$ near the domain top. There are 58 vertical levels, giving a physical domain height of $24\,km$. A 5-km deep sponge layer is added to the upper part of the physical domain to reduce wave reflection. The mountain is introduced impulsively into the basic flow at $t = 0\,s$.

The basic flow and orographic parameters, as well as their special characteristics are summarized in Table 1. Figure 1a and b shows *skew T-log p diagrams* of two idealized soundings, which have Convective Available Potential Energy (CAPE) values of approximately 2,000 and $1{,}000\,J\,kg^{-1}$, respectively. The sounding in Fig. 1a (with CAPE $\sim 2000\,J\,kg^{-1}$), which was described earlier, is used in most cases, and the other in Fig. 1b (with CAPE $\sim 1000\,J\,kg^{-1}$) is used for the sensitivity test. The difference in CAPE values results from the change in relative humidity (85% instead of 93% of relative humidity is used for the sounding in Fig. 1b). Case 1 is a dry flow, while Case 2, as well as the others, is a moist flow and serves as a control run. The sensitivity tests with different

Table 1. Characteristics of the numerical experiments

Case	V	F_w	Integration time (h)	Special characteristics	Figures	Flow regimes
1	15.0	NA	32	Dry, $F_d = 0.600$	Fig. 2	NA
2	15.0	0.666	32	CAPE $= 2000\,J\,kg^{-1}$	Fig. 3	II
3	7.50	0.333	64	Small F_w flow	Fig. 6	I
4	30.0	1.332	16	Large F_w flow	Fig. 7	III
2A	15.0	0.666	32	As case 2, but with a 15 km resolution	Fig. 5	II
2B	15.0	0.666	32	$f = 0\,s^{-1}$	Fig. 8	I/II
2C	15.0	0.666	32	As case 2, but with arc-shaped mountain	Fig. 10	II
2BC	15.0	0.666	32	As case 2, but with $f = 0\,s^{-1}$ and arc-shaped mountain	Fig. 12	I/II
3C	7.50	0.333	64	As case 3, but with arc-shaped mountain	Fig. 13	I
2D	15.0	0.661	32	As case 2, but with CAPE $= 1000\,J\,kg^{-1}$	Fig. 15	II
3D	7.50	0.330	64	As case 3, but with CAPE $= 1000\,J\,kg^{-1}$	Fig. 15	II

*$N_w = 0.01127\,s^{-1}$, CAPE $= 2000\,J\,kg^{-1}$, $h = 2\,km$, and $a = 100\,km$ for all cases, except for cases 2D and 3D, where CAPE $= 1000\,J\,kg^{-1}$ and $N_w = 0.01135\,s^{-1}$

moist Froude numbers, F_w, are conducted to help identify the three-dimensional moist flow regimes, and the number (F_w) varies with the basic flow (U) (Cases 3 and 4). Note that in order to keep symbols consistent with other studies, the basic wind speed from the south is represented by U, instead of V. Case 2A is designed to examine the influence of model resolutions. The effect of the Coriolis force (Cases 2B and 2BC), different mountain geometries (Cases 2C, 2BC, and 3C), and the CAPE (Cases 2D and 3D) are also examined. The time step is 40 s for Case 2A and 60 s for the others. The model is integrated for a nondimensional time (Ut/a) of 17.28.

3. Three-dimensional moist flow regimes and dynamics

In order to test the model and better understand the complicated moist flow dynamics, we first conduct an experiment for a rotating (*f*-plane), dry flow over a 3D ridge-like mountain (Case 1). At $Ut/a = 17.28$ $(t = 32\,h)$, a surface high pressure exists along the southwestern slope of the mountain, while a low pressure exists along the northeastern slope of the mountain (Fig. 2a). This high-low pressure couplet is associated with the leftward (rightward) turning of the upstream (downstream) flow (Fig. 2b). Flow splitting can be seen clearly from the figure, and the stagnation point is located over the eastern upslope, instead of at the middle point for a non-rotating flow, similar to that simulated in Schneidereit and Schär (2000). Facing downstream (i.e., northward), the upstream (downstream) flow accelerates leftward (rightward) in order to adjust to the reduced (increased) Coriolis force in response to the reduced (increased) horizontal velocity upstream (downstream) (see e.g., Smith, 1979). In the absence of the Coriolis force, the high-low pressure perturbation couplet would be symmetric with respect to $x = 0\,km$. Another high pressure is produced on the left side downstream of the mountain (Fig. 2a); it is separated from the first high on the windward side and propagates through the western edge of the obstacle to the leeside.

When the low-level flow approaches the obstacle, it splits on the eastern (right) side of the foothills but tends to cross over the ridge from the western (left) side, as shown in the potential temperature field in Fig. 2b. On the leeside, the flow is very asymmetric and converges to the eastern side 600 km downstream from the ridge. The flow along the eastern edge of the mountain is less disturbed while it accelerates around the western slope due to the leftward turning of the upstream flow (Fig. 2c). This accelerated east–southeasterly flow near the foothills of the topography may be referred to as barrier winds (Pierrehumbert and Wyman, 1985), which induces strong upslope convergence near the west surface. This feature of the flow response has also been found in other studies of flow over the Alps (Stein, 2001) and over the Central Mountain Range of Taiwan (Lin et al, 1992; Chen and Li, 1995; Li et al, 1997). The dynamics of barrier wind formation may be found in standard textbooks or review papers (Smith, 1979) and will not be repeated here.

The vertical motion at the first half σ level $(z \approx 30\,\text{m})$ is upward over the windward slope and downward over the lee slope (Fig. 2c), as anticipated, and a foehn-like strong downslope wind ($\sim 40\,ms^{-1}$) is produced at the lee side of the mountain. This strong downslope wind is very warm, as can be seen from Fig. 2d. On the upslope, the southeasterly barrier jet, forced by the mountain and Coriolis force, shifts its flow regime from flow-around on the eastern upslope to flow-over on the western upslope. This is similar to those simulated by Olafsson and Bougeault (1997). This asymmetry of barrier wind over the upslope can be explained by the presence of a mountain anticyclone (Smith, 1979). Above the lee slope, the vertical velocity at higher levels shows a repeated U-shaped pattern, which is an indication of upward-propagating mountain waves (Smith, 1980). These waves may be classified as rotating, hydrostatic mountain waves since $1 \ll Na/U < N/f$, where $N = 0.0123\,s^{-1}$, $a = 100\,km$, and $U = 15\,ms^{-1}$, which gives $Na/U = 82$ and $N/f = 123$ (Queney, 1948; Smith, 1979). The vertical wavelength predicted by the linear theory (Queney, 1948) is $2\pi U/N = 7.7\,km$, which is about the same as that simulated by the model (Fig. 2d).

3.1 Moist flow regimes

Figure 3 shows simulation results for a moist airflow $(F_w = 0.666)$ over a 3-D ridge-like

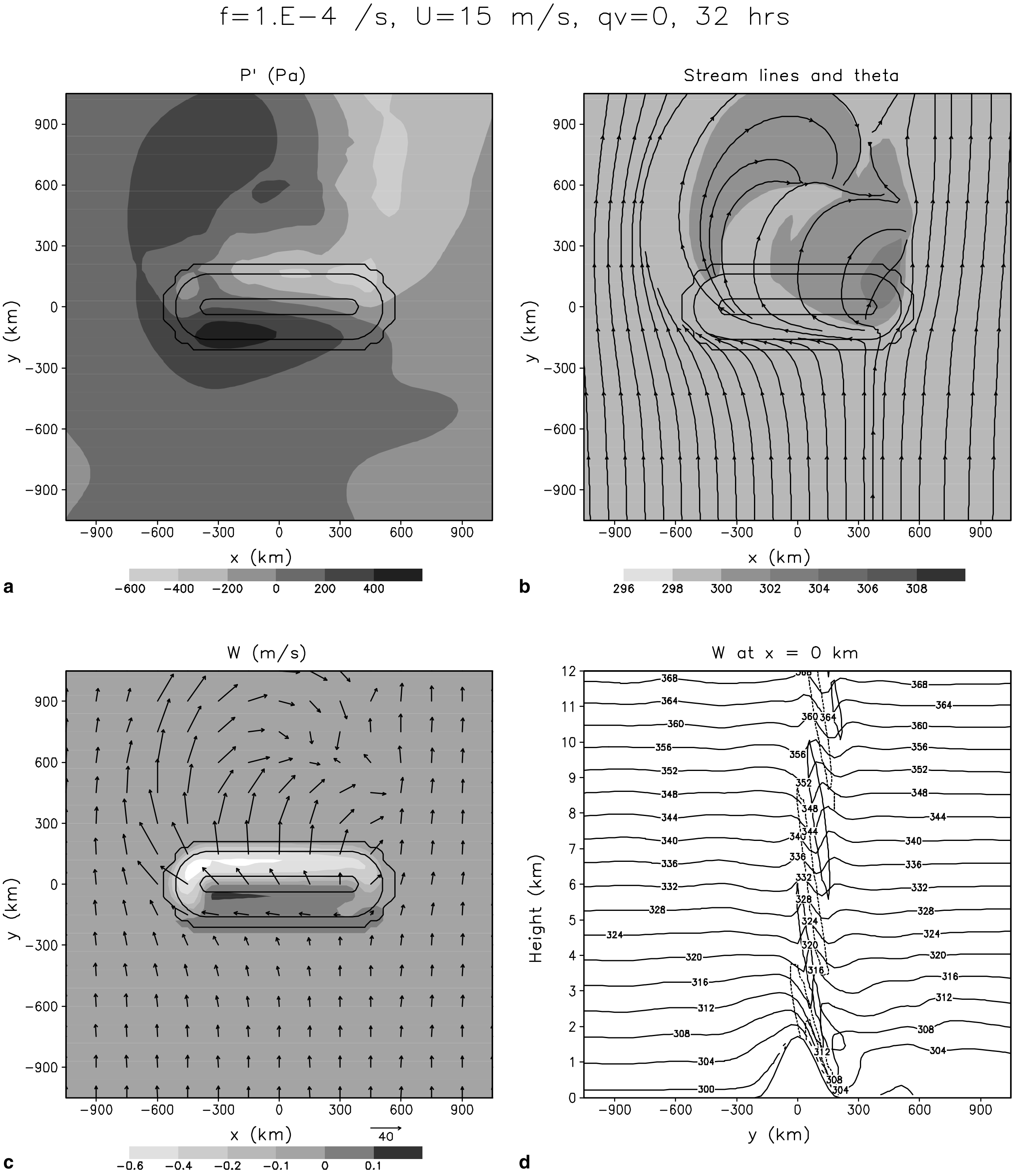

Fig. 2. Simulated dry airflow over the ridge-like mountain (Case 1) for $U = 15\,ms^{-1}$ and $f = 10^{-4}\,s^{-1}$ at $Ut/a = 17.28$; (**a**) Surface pressure perturbation (in *Pa*), (**b**) potential temperature (shaded; in K) and streamlines at the first half sigma level, (**c**) the vertical velocity, *w*, (shaded; in ms^{-1}) and horizontal wind vectors at the first half sigma level, and (**d**) *w* (in ms^{-1}) and potential temperature (in K) along the north–south cross section of $x = 0\,km$. The other dimensional parameters are: $a = 100\,km$, $h = 2\,km$, and $t = 32\,h$. The terrain contours in (**a**)–(**c**) are 0, 200, and 1800 m. The plotting domain is a subdomain of the actual computational domain

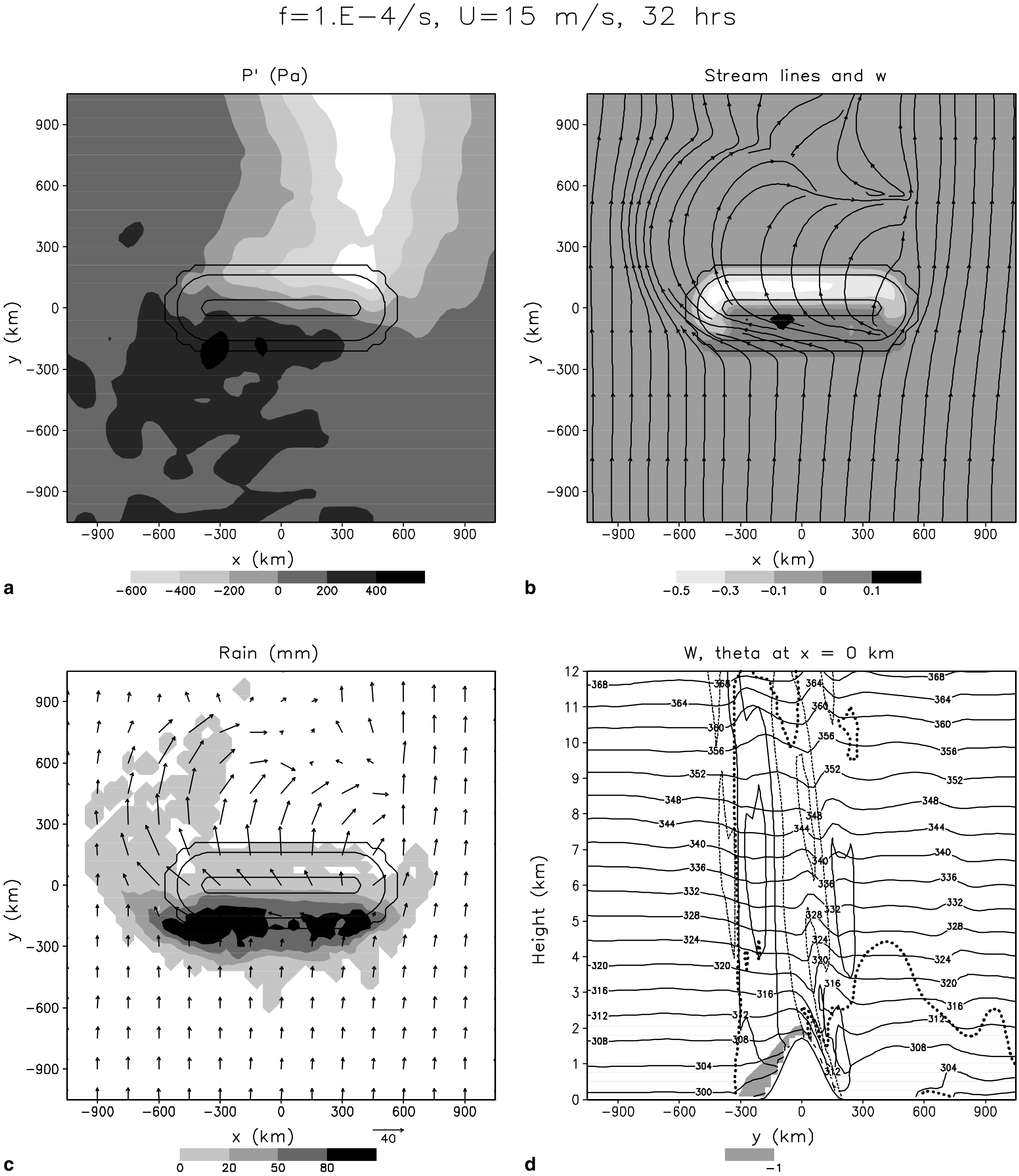

Fig. 3. Simulated moist airflow over the ridge-like mountain (Case 2) at $Ut/a = 17.28$. (**a**) The surface pressure perturbation (in *Pa*), (**b**) w (shaded; in ms^{-1}) and streamlines at the first half sigma level, (**c**) the surface accumulated rainfall (shaded; in mm) and horizontal wind vectors at the first half sigma level, and (**d**) w (in ms^{-1}) and potential temperature (in K) along the north–south cross section of $x = 0\,km$. The flow and orographic parameters are $U = 15\,ms^{-1}$, $N_w = 0.01127\,s^{-1}$, $h = 2\,km$, $F_w = 0.666$ and $f = 10^{-4}\,s^{-1}$. In (**d**), the cloud boundary is denoted by thick dotted curve for total water content greater than $0.0005\,g\,kg^{-1}$, and the cold pool is shaded by $\theta' < -1\,K$

mountain at $Ut/a = 17.28$ (Case 2). The dimensional integration time and basic flow speed are $32\,h$ and $15\,ms^{-1}$, respectively. Other flow and orographic parameters can be found in Table 1. After a 8.64 nondimensional time ($t = 16\,h$) simulation, the system has reached a quasi-steady state in terms of the precipitation rate and the movement of the system. Similar to the dry flow (Fig. 2a), a high-low pressure perturbation couplet straddles the mountain (Fig. 3a) due to the influence of the mountain and the Coriolis force. However, the high-pressure perturbation upstream of the mountain is more scattered due to the presence of the mesoscale convective system (MCS) over the upslope of the mountain, while the leeside low-pressure perturbation is less affected (i.e., less scattered).

Upstream of the MCS, the flow is deflected slightly to the right, which then turns westward to become an east–southeasterly barrier wind over the windward slope (Fig. 3c). Around $y = -300$ km, a convergence zone is detected and this convergence appears to be produced by the upward motion associated with the MCS (Chen and Frank, 1993). The low-level streamline patterns with (Fig. 2b) and without (Fig. 3b) moisture are very similar; however, the anticyclonic circulation downstream of the mountain is more confined for the moist case, and the flow has been modified by the upstream convective system. Note that the wider range of the anticyclonic circulation for the dry case is due to the downstream-propagating high. A broad region of upward motion is produced along the windward (south) slope of the idealized mountain, with a maximum located to the western portion of the upslope (Fig. 3b). This maximum region of upward motion is produced by the convergence of the southeasterly barrier winds, forced by the Coriolis force, and the southerly basic wind.

The accumulated precipitation area is arc-shaped with the left arm (facing downstream) extending to the northwest side of the isolated topography (Fig. 3c). This arc-shaped convective line is similar to rainbands observed in Hawaii under a low-Froude number flow. The Hawaiian rainbands tend to propagate outward from the island (see Fig. 2 of Smolarkiewicz et al, 1988) and are generated by local convergence due to the interaction of the trade winds with the orographic density current produced by nocturnal cooling. The coverage of the rainfall area extends upstream to a distance of $330\,km$ from the ridgeline (Fig. 3c), and the maximum accumulated amount is more than $90\,mm$ by 17.28 nondimensional time ($32\,h$). Compared with grid-scale clouds, the subgrid-scale convections dominate the rainfall and precipitate at a lower elevation and farther upstream of the flow (not shown). A maximum rainfall is located on the western upslope and is co-located with the maximum upward motion (Fig. 3b).

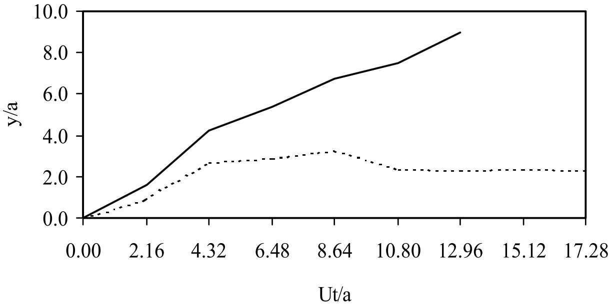

Fig. 4. Upstream propagating distances of the mesoscale convective system (MCS) versus time: dashed line for Case 2 with $F_w = 0.666$ ($U = 15\,ms^{-1}$) and solid line for Case 3 with $F_w = 0.333$ ($U = 7.5\,ms^{-1}$)

A cold pool, which is depicted by $\theta' < -1\,K$, is produced over the windward slope by the MCS (Fig. 3d). The orographically generated MCS develops rapidly and propagates upstream at an average speed of $6.9\,ms^{-1}$ over a 6.48 nondimensional time (12 h) period, yielding a nondimensional propagation speed of about 0.51 (Fig. 4). After a 6.48 nondimensional time simulation, the MCS, ahead of the cold pool, reaches its quasi-stationary state. Thus, this moist flow response may be characterized as a regime with quasi-stationary upslope convective systems (i.e., Regime II of Chu and Lin, 2000). The difference between the present three-dimensional (3-D) moist flow regime and the two-dimensional (2-D) flow regime by Chu and Lin (2000) is that the heavy rainfall is located over the upwind slope instead of over the mountain peak and, more importantly, is directly related to the presence of the high wind speed. This finding is important since it is more consistent with observations (Lin et al, 2001). The high wind speed does not prevent the maximum rainfall from being located over the windward slope. On the lee slope, a foehn-like downslope wind is also produced (Fig. 3d), similar to that in dry case (Fig. 2d) and previous studies (Schneidereit and Schär, 2000).

Case 2A, which uses a grid spacing of 15 km, is conducted to examine the influence of horizontal resolutions on heavy orographic rainfall simulations. The patterns of simulated streamlines and low-level vertical velocity (Fig. 5a) are very similar to those with a resolution of 30 km in Case 2 (Fig. 3b). The rainfall area is more compact and close to the foothills. This implies that a more stationary upslope convective system is actually developed with the higher resolution. As anticipated, the maximum amount of accumulated rainfall is larger because of the use of a higher grid resolution and more stationary system (i.e., it precipitates at the same location for a longer period of time). The east–southeasterly barrier winds and downstream anticyclone are also comparable for Cases 2 (Fig. 3c) and 2A (Fig. 5b). Although the simulated results from both cases are slightly different, the simulation with a 30 km resolution is capable of reproducing the main features of the MCS produced by that with a higher resolution. We therefore conclude that a 30 km resolution is adequate for this heavy orographic rainfall study.

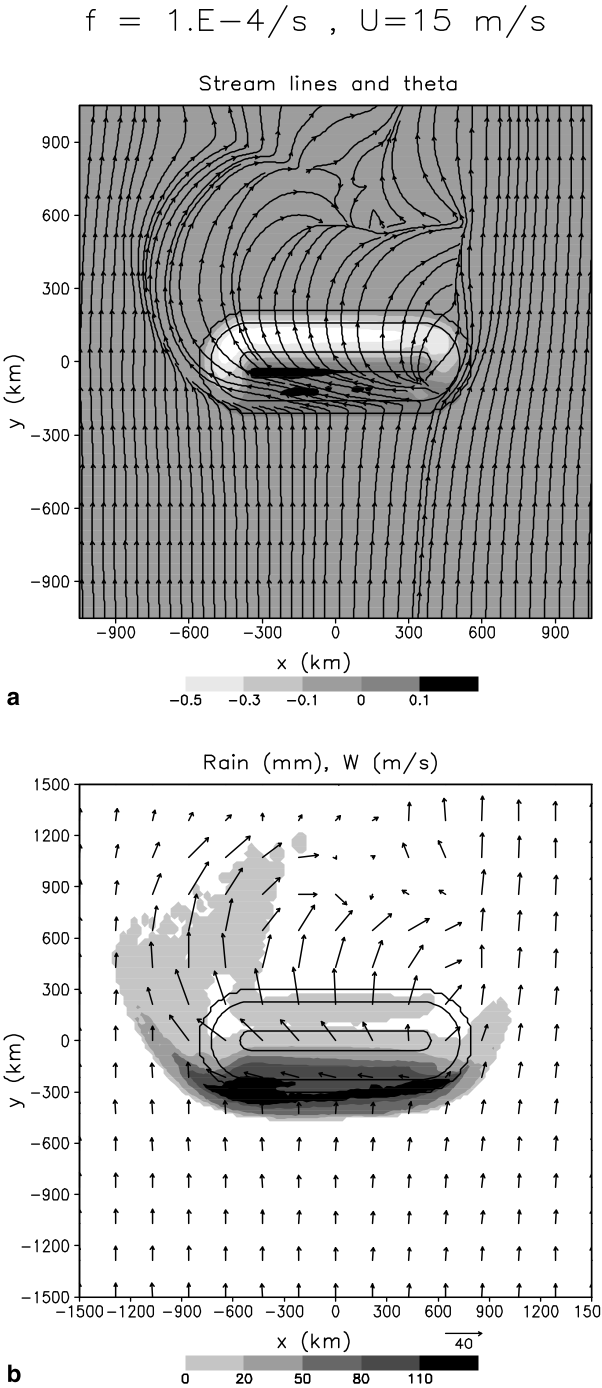

Fig. 5a. The vertical velocity (shaded; in ms^{-1}) and streamlines at the first half sigma level, and (**b**) the surface accumulated rainfall (shaded; in *mm*) and first half sigma level horizontal wind vectors for Case 2A with a resolution of 15 *km* after $Ut/a = 17.28$ (32 h) integration

Figure 6 shows the model simulation results at the first half σ surface ($z \sim 30$ m) for Case 3 at $Ut/a = 17.28$ (64 h). The moist Froude number (F_w) for this case is 0.333, and the basic wind speed is $7.5\, ms^{-1}$. Other relevant flow and orographic parameters can be found in Table 1. The pressure perturbation (not shown) is similar to those simulated in Case 2 (Fig. 3a); however, the high pressure upstream is able to propagate downstream from the western side of the obstacle as it does in the dry case (Fig. 2a). Note that the Rossby number ($R_o \approx 0.375$) is about half that of Case 2. As anticipated, for this smaller Rossby number flow, the deflection of the horizontal easterly wind with respect to the southerly wind upstream of the foothills is relatively stronger (in a nondimensional sense) than that in Case 2, and the flow tends to move around the mountain. Flow splitting can also be clearly seen from the horizontal wind vectors (Fig. 6b), also indicating that the mountain blocks a significant amount of the incipient upstream flow. Unlike Case 2, no severe downslope wind or wave breaking form over the lee slope due to the horizontal deceleration of the upstream flow (Fig. 6d).

After a 4.32 nondimensional time (16 h) simulation in Case 3, a meso-β cyclonic vortex is located northeast of the mountain, while an anticyclonic vortex is located northwest of the mountain (not shown). This pair of lee vortices

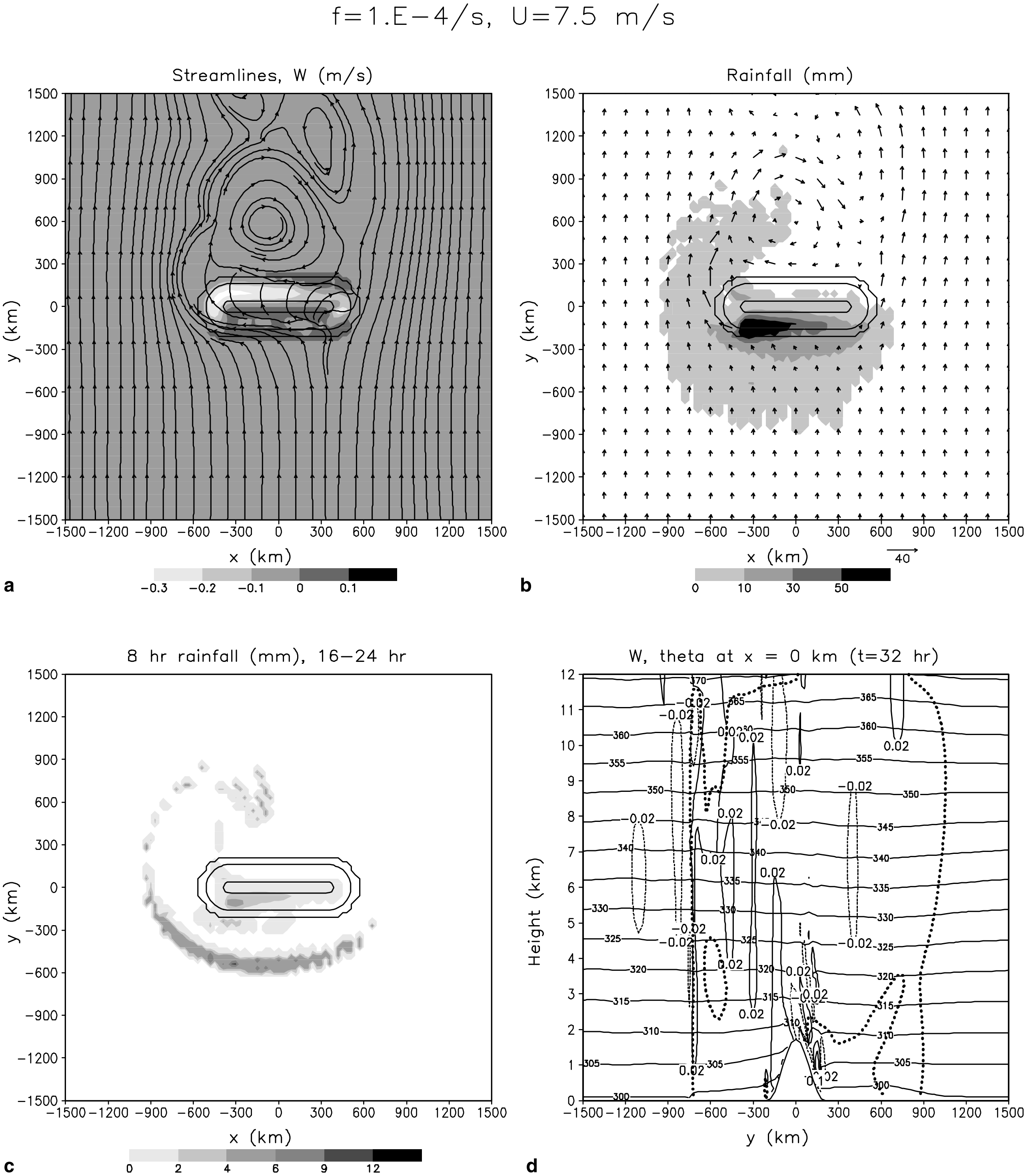

Fig. 6. (Case 3) (**a**) The 17.28 nondimensional time (64 h) simulated w (shaded; in ms^{-1}) and streamlines at the first half sigma level, (**b**) 17.28 nondimensional time (64 h) simulated horizontal wind vectors at the first half sigma level and the surface accumulated rainfall (shaded; in mm), (**c**) 8-hr accumulated rainfall from $Ut/a = 4.32$ to $Ut/a = 6.48$ (16- to 24-h), and (**d**) w (in ms^{-1}) and potential temperature (in K) along the north–south cross section of $x = 0\,km$ for Case 3 after $Ut/a = 8.64$ (32 h) integration

is similar to those produced over an isolated, circular mountain in an inviscid, non-rotating, low-Froude number flow (Smolarkiewicz and Rotunno, 1989) which has $R_o = \infty$, but are modified here by the Coriolis force and latent heating. The formation of this pair of lee vortices is similar to that simulated in Lin et al (1992). In fact, the northeastern cyclonic vortex is associated with a strong low-pressure region and may subsequently develop into a mesoscale lee cyclone similar to the mesocyclones found to the southeast of Taiwan under a southwesterly monsoon flow (Sun et al, 1991; Lin et al, 1992). During the last half of the simulation, the anticyclonic vortex moves to the center of the leeside of the mountain, while the cyclonic vortex propagates farther downstream (Fig. 6a). In other words, vortex shedding is produced. The rainfall maximum is located on the western upslope (Fig. 6b), similar to Case 2 (Fig. 3c), due to the southeasterly barrier winds.

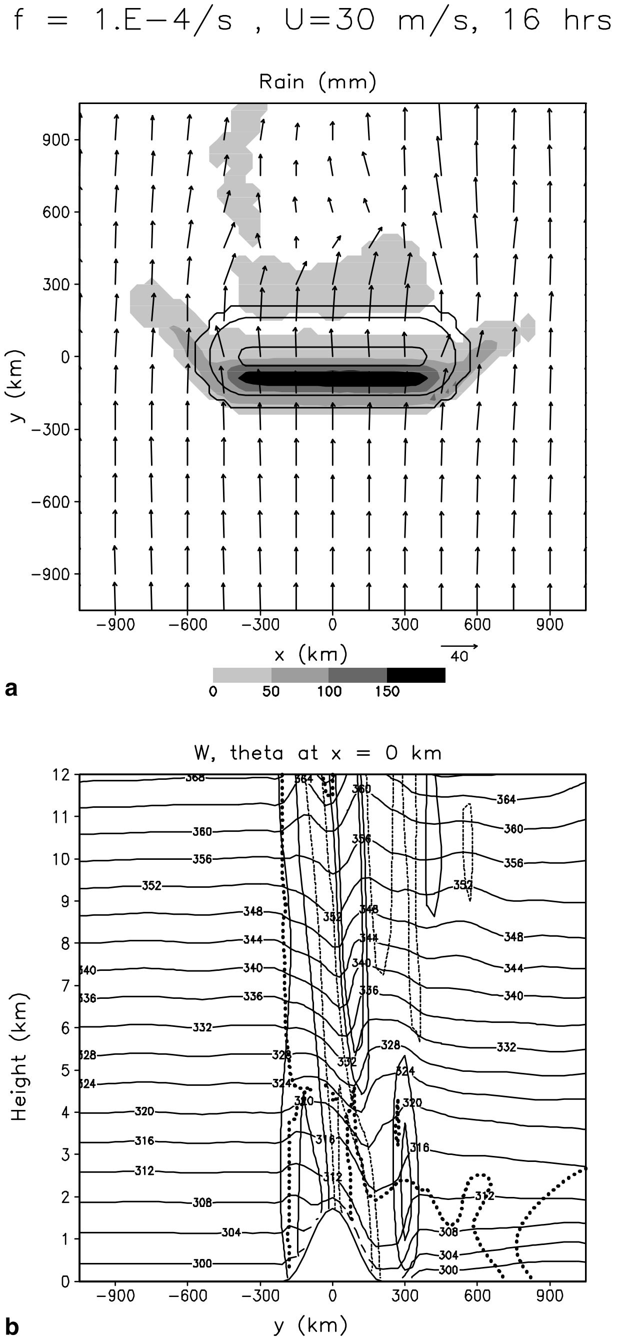

Fig. 7a. The surface accumulated rainfall (shaded; in *mm*) and horizontal wind vectors at the first half sigma level, and (**b**) w (in ms^{-1}) and potential temperature (in K) along the north–south cross section of $x = 0\,km$ for Case 4 after a 17.28 nondimensional time (16 h) simulation

Figure 6c shows 2.16 nondimensional time (8 h) accumulated rainfall, which indicates that an orographically generated MCS develops and propagates upstream, while a quasi-stationary convective system develops near the upstream western slope, where the maximum accumulated rainfall is located. The western upslope convective system is generated by the convergence of the barrier wind and the southerly basic wind, and the maximum accumulated rainfall is more than 70 mm by the nondimensional time of 17.28 (64 *h*). The upstream-propagating MCS moves at a speed of $5.2\,ms^{-1}$ ($=0.69$ nondimensional propagation speed, Fig. 4) and dissipates after 12.96 nondimensional time (48 h) simulation at $y=-900$ km. The flow response for Case 3 may be characterized as the regime with a quasi-stationary upslope convective system and an upstream-propagating convective system. On the cross section of $x=0$ km after a 8.64 nondimensional time (32 h) simulation, it can be seen that the leading edge of the cold pool (i.e., the MCS) has advanced to about $y=-750$ km ($\theta=300$ K). The disturbance over the lees slope is weaker compared to that in Case 2 (Fig. 3d).

In Case 4, with F_w increased to 1.332 ($U = 30\,ms^{-1}$), the flow behaves quite differently. The total nondimensional integration time is still 17.28, which now corresponds to the dimensional time of 16 *h*. There is no apparent horizontal deflection of the basic flow except near the eastern and western edges of the mountain (Fig. 7a). A convergence line associated with cyclonic vorticity is produced $\sim$500 km downstream of the obstacle. This lack of upstream turning is mainly caused by a higher Rossby number flow ($U/fL \approx 1.5$ where $U = 30\,ms^{-1}$, $f = 0.0001\,s^{-1}$, and $L=200$ km), so that rotational effects are essentially negligible. A strong convective system is produced over the windward side and stays on the upslope during the whole simulation, while another convective system is generated on the lee side due to the hydraulic jump-like feature and reaches a quasi-steady state after a 12.96 nondimensional time (12 h) simulation (Fig. 7b). Unlike Case 2 (Fig. 3c), the rainfall pattern is quite symmetric with respect to $x = 0$ due to negligible turning by the Coriolis force. The maximum rainfall over the upslope reaches 180 mm by 17.28 nondimensional time (Fig. 7a), and both grid-scale and subgrid-scale rainfall amounts are comparable in this case (not shown) due to strong upward motion produced by the orographic lifting of the strong basic flow. The flow response in this case may be characterized as a regime with a stationary upslope convective system and a quasi-stationary downstream convective system. Note that this flow regime is different from the Regime III classified by Chu and Lin (2000) in which the downstream convective system keeps propagating. Although a strong low-level jet of magnitude $U = 30\,ms^{-1}$ is rarely observed upstream of the Alps, this type of flow is not unrealistic for other mountain ranges in terms of the nondimensional moist Froude number. Note that a rainfall amount of 180 mm in 17.28 nondimensional time (16 h) is much heavier than that predicted by the control case $(U = 15\,ms^{-1})$, which is 90 mm in the same nondimensional time (32 h). The heavy rainfall is attributed to the much stronger orographic lifting, which can be roughly estimated by $w_{oro} \approx U\partial h/\partial x \approx 0.3\,ms^{-1}$, for triggering the conditional or convective instability. Even though a mesoscale convective system is advected to the lee side, the upslope quasi-stationary MCS is able to produce very heavy rainfall there. This is also consistent with the ingredient argument proposed by Lin et al (2001), which includes a LLJ as an ingredient for heavy orographic rain.

3.2 Effects of the Earth's rotation, mountain geometry, and CAPE

As mentioned in the introduction, the flow over the Alps is strongly influenced by the Coriolis force (Schneidereit and Schär, 2000) and heavy orographic rainfall events often start in the concave region over the southern slopes of the Alps, such as in the Lago Maggiore, Ticino and Piedmont areas, under southerly or southeasterly low-level flows (Binder and Schär, 1996; Buzzi and Foschini, 2000). In this subsection, we investigate the impacts of the Coriolis force and concave mountain geometry in a much simpler

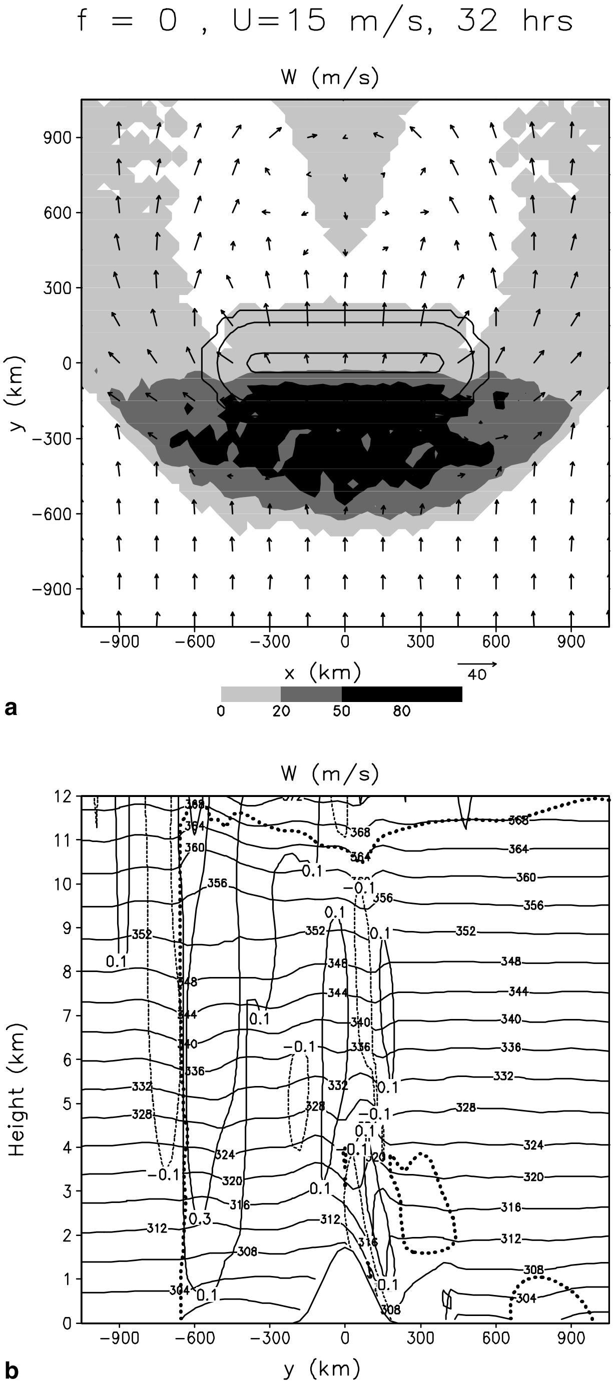

Fig. 8a. The surface accumulated rainfall (shaded; in mm) and horizontal wind vectors at the first half sigma level, and (**b**) w (in ms^{-1}) and potential temperature (in K) along the north–south cross section of $x = 0\,km$ for Case 2B $(f = 0\,s^{-1})$ after a 17.28 nondimensional time (32 h) simulation

fashion than that addressed in Schneidereit and Schär (2000) (which includes a finite width of LLJ) or in Rotunno and Ferretti (2001) (which includes a horizontal moisture gradient). In addition, we also investigate the effects of CAPE on the orographically induced MCS.

We perform a sensitivity test to investigate the effects of the Earth's rotation for an intermediate Froude number flow ($F_w = 0.666$) by deactivating the Coriolis force (Case 2B). Without rotation, it is clearly shown in Fig. 8a that the low-level horizontal wind is symmetric with respect to the centerline ($x = 0\,km$). A significant portion of the upstream flow is blocked by the mountain as compared to the corresponding rotating case (wind vectors in Fig. 3c), while the rest of the flow splits symmetrically toward both the eastern and western edges of the mountain range. The cold pool advances to $y = -600\,km$ (Fig. 8b), which is about 300 km farther upstream compared with the case with rotation, i.e., Case 2 (Fig. 3d). There are two symmetric vortices formed downstream of the mountain ($\sim y = 700\,km$). Unlike the corresponding rotating case (Case 2), no east–southeasterly barrier winds form at the foothills or over the upwind slope of the mountain. The simulated MCS is quasi-stationary at upstream foothills in the rotational case. From Figs. 8b and 9 (difference fields of rainfall and horizontal wind vectors between Case 2 and 2B), we also can see that a simulated MCS propagates far upstream and another weak convective system stays close to the top of the upslope. Thus, we conclude that the Coriolis force helps part of the upstream flow to make a transition to a higher number flow regime (i.e., from "flow-around" to "flow-over") by deflecting the incipient southerly flow to be southeasterly barrier winds and produce heavier rainfall over the western portion of the windward slope in Case 2. Again, this anticyclonic turning of the upslope wind can be explained by the mountain anticyclone (Smith, 1979).

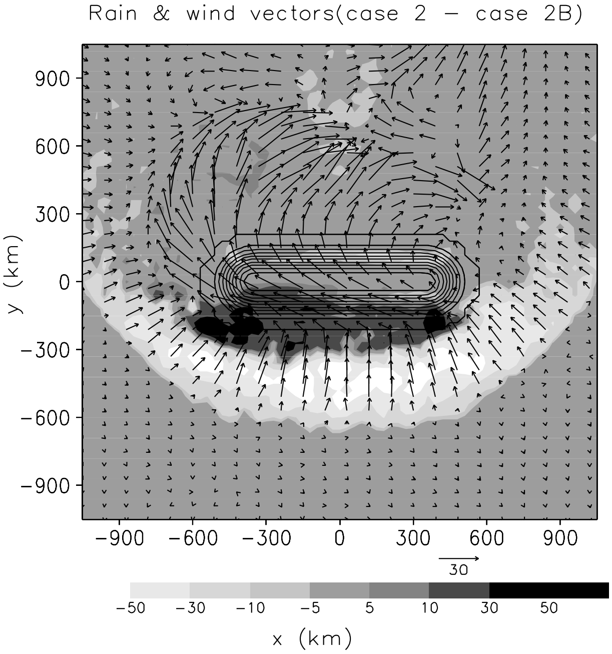

Fig. 9. Difference fields in horizontal wind vectors and surface accumulated rainfall (shaded; in *mm*) for Case 2 – Case 2B after a 17.28 nondimensional time (32 h) simulation

In order to investigate the effects of Alpine mountain geometry, we add a western flank to the main east–west ridge (Case 2C), identical to that used by Schneidereit and Schär (2000), but with a horizontally uniform high wind speed, instead of a finite-width LLJ. Figure 10a shows the vertical velocity and streamline fields near the surface. The maximum vertical velocity is located in the concave region. However, heavy rainfall regions are shifted to the southern slope of the western flank of the mountain and the whole upslope of the east–west main ridge with the maximum located at the eastern upslope (Fig. 10b). This behavior is very different from that simulated in the case without a western flank mountain which gives maximum rainfall over the western upslopes (Fig. 3c; Case 2). The maximum accumulated rainfall reaches a value over 100 mm, comparable to the case with topography without a western flank (Fig. 3c; Case 2). Schneidereit and Schär (2001) did indicate that the rainfall maximum over the upslope does depend on the location of the finite-width LLJ. Another major difference between Cases 2C and 2 is that the convective system upstream of the main east–west main ridge have advanced to be farther upstream at $y \approx -600\,km$ (rainfall in Fig. 10b and cloud field in Fig. 10c), compared to $y \approx -300\,km$ in Case 2 (Figs. 3c and d). This advancement of the convective system results from the deceleration of the moist flow on the inner slopes of the arc-shaped mountain, as can be seen by comparing the accumulated rainfall amount and distribution at 17.28 nondimensional

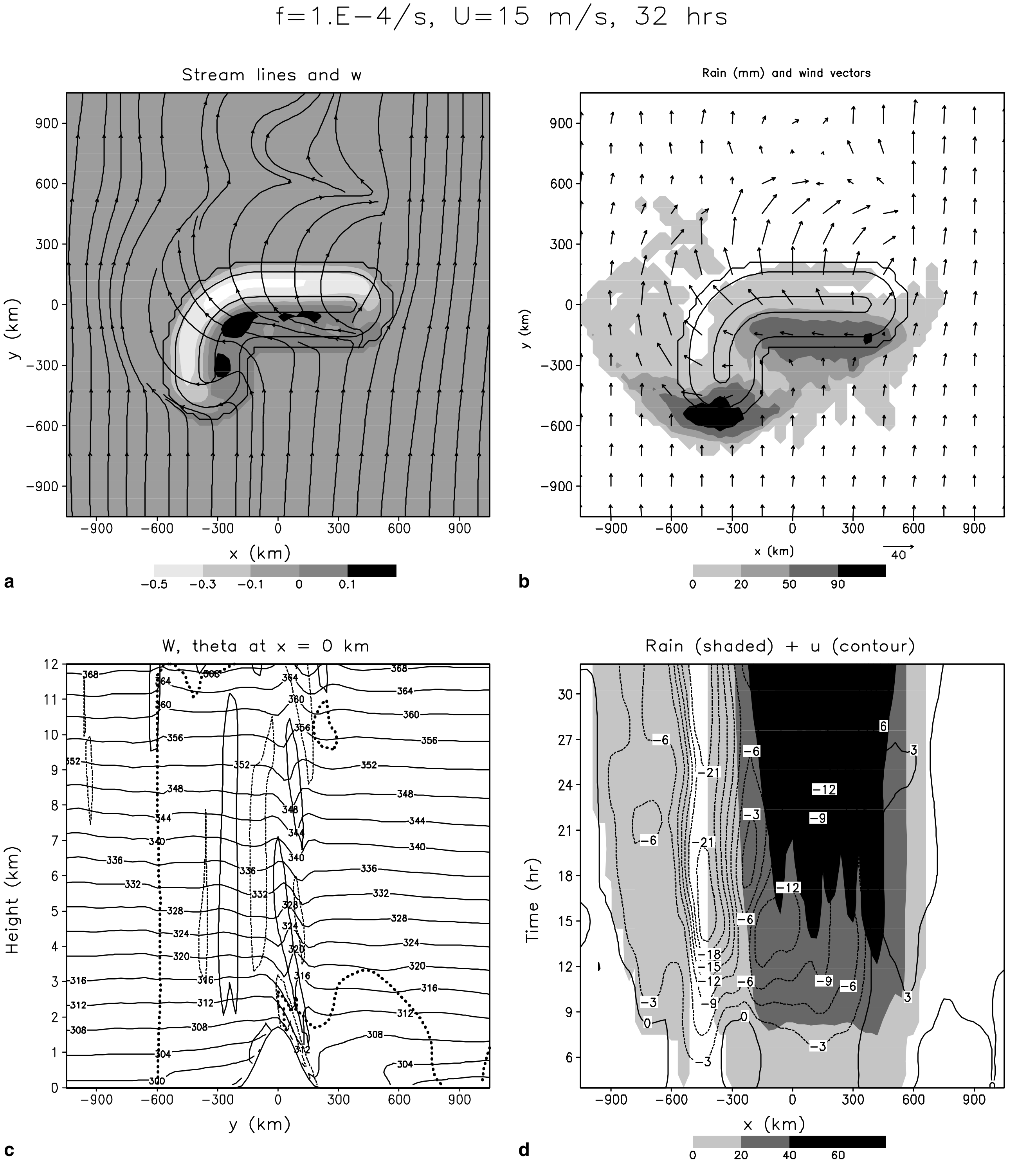

Fig. 10. Simulated moist airflow over an arc-shaped mountain (Case 2C) for $F_w = 0.666$ ($U = 15\,ms^{-1}$) at $Ut/a = 17.28$ (32 h); (**a**) Streamlines and w (shaded; in ms^{-1}) at the first half sigma level, (**b**) accumulated rainfall (shaded; in *mm*) and the horizontal wind vectors at the first half sigma level, (**c**) w (in ms^{-1}) and θ (in K) on the vertical cross section of $x = 0\,km$, and (**d**) time evolution of accumulated rainfall (shaded; in *mm*) and u (in ms^{-1}) at $y = -180\,km$

time (32 h; Fig. 10b) and 4.32 nondimensional time (8 h; Fig. 11a). Note that different precipitation grey scales are used in Figs. 10b and 11a. The blocking of the eastern slope of the western flank can also be seen from the time evolution of the u wind at $y = -180\,km$ (Fig. 10d). The westward-

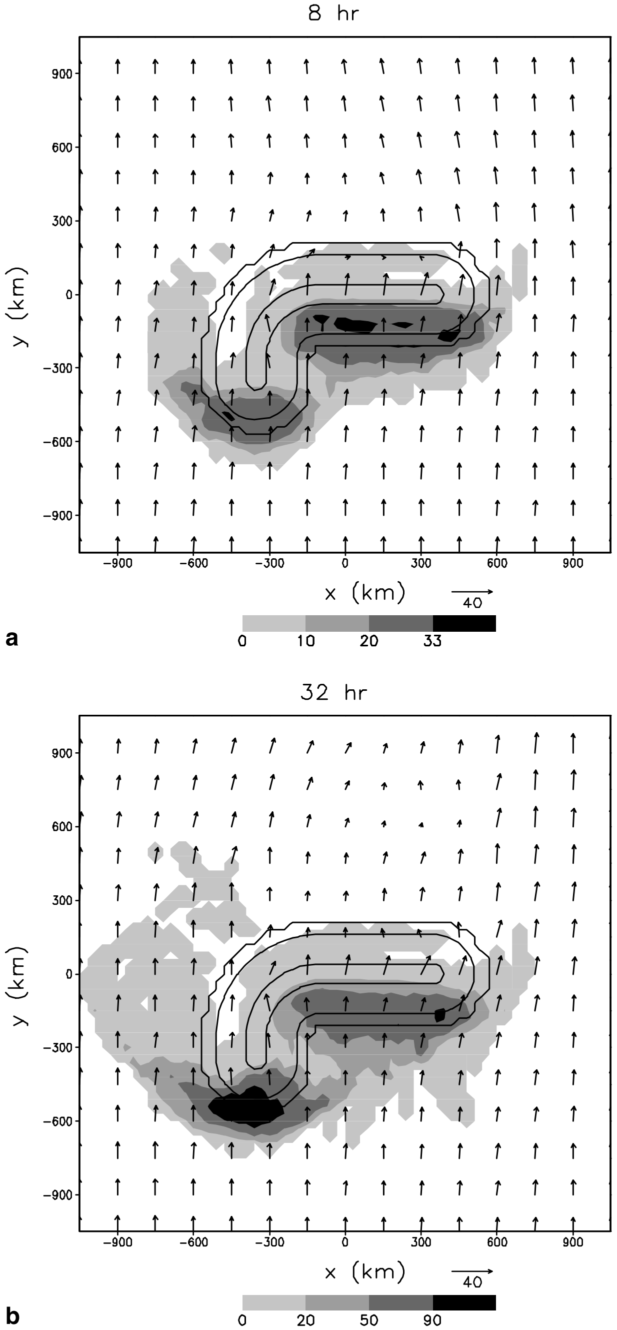

Fig. 11a. Horizontal wind vectors at $z = 3\,km$ and accumulated rainfall (shaded; in mm) at the surface at $Ut/a = 4.32$ (8 h) for Case 2C, and (**b**) same as (**a**) except at the nondimensional time of 17.28 (32 h). Note that different precipitation classes are used

deflected southerly wind on the western flank at the foothills (e.g., $x = -150\,km$) reaches its maximum of about $u = -15\,ms^{-1}$ at about 8.1 nondimensional time (15 h) and gradually weakens to about $u = -9\,ms^{-1}$ after 12.96 nondimensional time (24 h). In summary, this weakening of the southeasterly barrier wind is produced by the blocking of the western flank. This, in turn, helps the convective system move outward and the maximum rainfall on the upslope of the main ridge to shift eastward. The subgrid-scale rainfall has its maximum near the concave region (not shown), corresponding to the maximum upstream low-level vertical velocity (Fig. 10a), while the grid-scale rainfall is more widely distributed on the southern slopes of the mountain. Thus, the rainfall maximum might be enhanced and located nearer to the concave region if a finer grid-scale is used. Due to the limitation of the WRF model, which does not have nesting capability at this stage, we will leave the test of high-resolution simulations to a future study. Figure 11 shows the wind vector fields at $z = 3\,km$ for Case 2C at 4.32 nondimensional time (8 h) and 17.28 nondimensional time (32 h). The flow is not disturbed much by the western flank, while split slightly over the main ridge and then converges on the lee side. The disturbance tends to propagate downstream. The disturbance by the mountain and convective systems at this level is much weaker than that near the surface. This implies that the disturbance in the lower layer dominates the flow response.

Figure 12a shows the vertical velocity and horizontal streamlines at $Ut/a = 17.28$ for Case 2BC (with $f = 0\,s^{-1}$). Without rotation, the flow produces upward vertical motion over the inner slope of the mountain without an obvious maximum location. Instead of two symmetric vortices, there is only one vortex downstream of the major mountain ridge. Figure 12b shows the accumulated rainfall and low-level horizontal wind vector fields. Due to the lack of Earth's rotation, the flow which splits to the left and right, experiences more deceleration and produces less rainfall on the upslopes, compared to that of the rotational case (Case 3C). The MCS propagates upstream, similar to that in Regime I as proposed by Chu and Lin (2000). Thus, the lack of rotation tends to shift the flow to a lower-number regime.

Figure 13 shows the flow fields for Case 3C with $F_w = 0.333$, $U = 7.5\,ms^{-1}$ at $Ut/a = 17.28$ (64 h). The basic dynamics is similar to that of Case 2C (Fig. 10) except the rainfall is more focused near the concave region. The maximum w is located at the concave region extending to

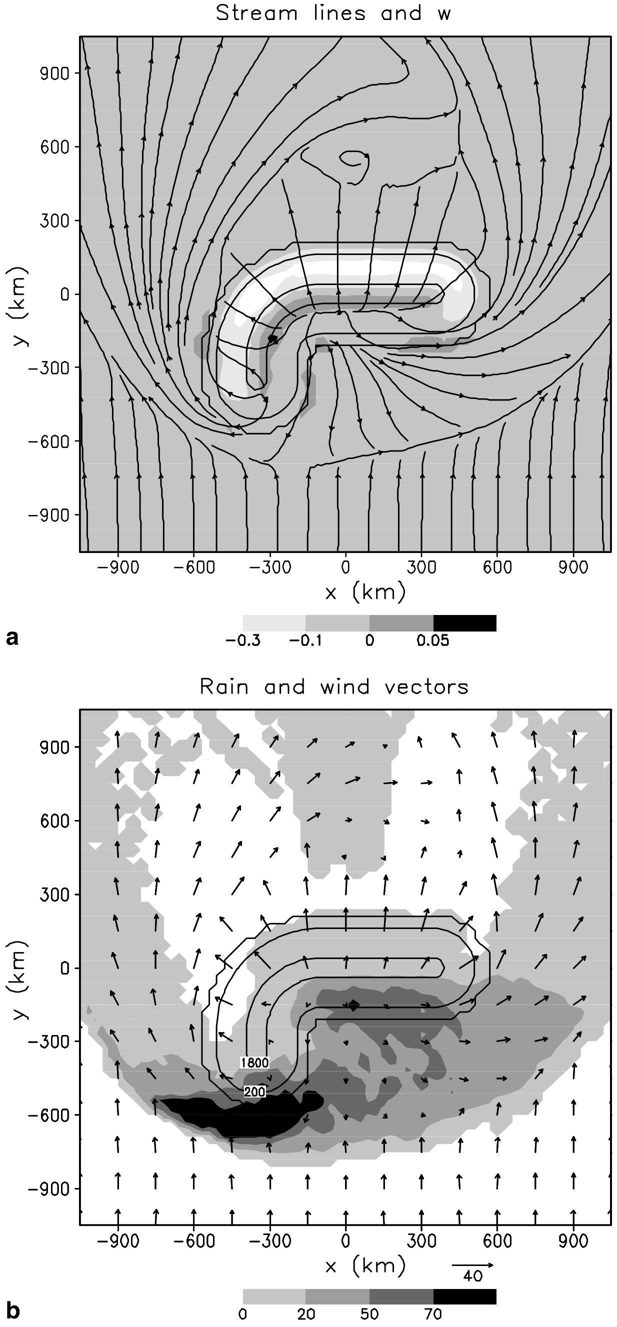

Fig. 12. Same as Fig. 10a and 10b, except for Case 2BC ($f = 0\,s^{-1}$)

the upslope of the western flank (Fig. 13a). Similar to Case 2C (Fig. 10b), a maximum rainfall region is located on the southern tip of the western flank in Case 3C (Fig. 13b). However, in contrast to Case 2C, there exists another rainfall maximum located near the concave region. This may be explained by the relatively stronger southeasterly barrier wind. The westward deflection of the basic wind near the concave region is relatively larger ($|u/U| \approx 6/7.5$; see Fig. 13d at $x = -150\,\mathrm{km}$.), compared to that in Case 2C ($|u/U| \approx 9/15$; see Fig. 10d at $x = -150\,\mathrm{km}$). Note that the southerly basic wind is denoted by U, instead of V, to be consistent with conventional symbols for defining the Froude number. The rainfall region extends farther upstream, such as $y \approx -950\,km$ (Fig. 13b), compared to that in Case 2C with a larger Froude number (Fig. 10b).

Figure 14 shows the first 4.32 nondimensional time (16 h) accumulated grid-scale (explicit) and subgrid-scale (parameterized) rainfall, respectively, for Case 3C with the arc-shaped mountain. The subgrid-scale rainfall is concentrated along the southwestern slopes of the main ridge and the southern edge of the western flank, while the grid-scale rainfall is concentrated over the concave area. The temporal evolution of the vertical velocity field indicates that the near-surface upward vertical motion starts near the concave region and remains there during the entire numerical simulation, while the simulated convective systems propagate outward from the concave region, i.e., they propagate upstream. It appears that the microphysical processes (resolvable rain) are able to react more directly to the upward vertical motion, which helps carry moisture upward to saturate the column. For numerical experiments with a finer grid resolution, the maximum rainfall may possibly shift closer to the concave region because this tends to increase the resolvable rainfall. The ratio of the maximum grid-scale rainfall to the subgrid-scale rainfall is increased in our simulations when the mean flow is stronger for both the ridge-like and arc-shaped mountain geometries.

In addition to the orographic lifting, evaporative cooling also plays an important role in forming the density current, which may generate new convective cells along its front edge. An ideal nondimensional parameter in determining the supercritical or subcritical flow with respect to the density current forcing is U/c_d, where c_d represents the propagation speed of the density current. When $U < c_d$ ($U > c_d$), the flow is subcritical (supercritical) with respect to the density current, and the density current is able (unable) to propagate upstream against the basic flow (Raymond and Rotunno, 1989). However, as remarked in Chu and Lin (2000), c_d is not an

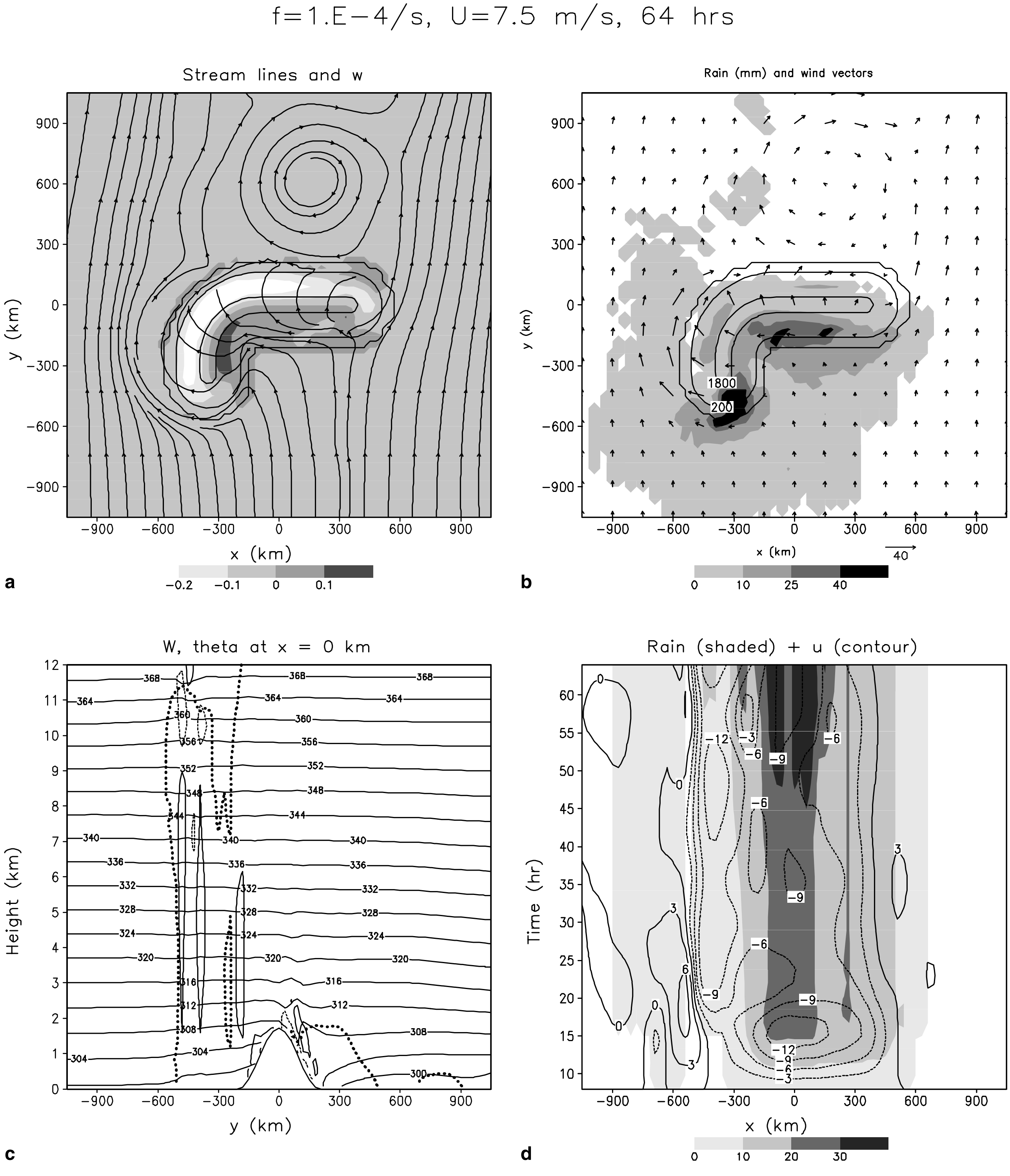

Fig. 13. Same as Fig. 10, except for Case 3C at $Ut/a = 17.28$ (64 h). The basic wind speed is $U = 7.5\,ms^{-1}$

easy parameter to estimate from a single vertical sounding. On the other hand, the strength of the evaporative cooling is closely related to the magnitude of CAPE in a conditionally unstable flow. Furthermore, the strength of a convective system is also well-represented by the CAPE if it is triggered by the conditional instability. Thus, in addition to the moist Froude number, we may use CAPE as a flow parameter to determine the location of a thermally forced convective system.

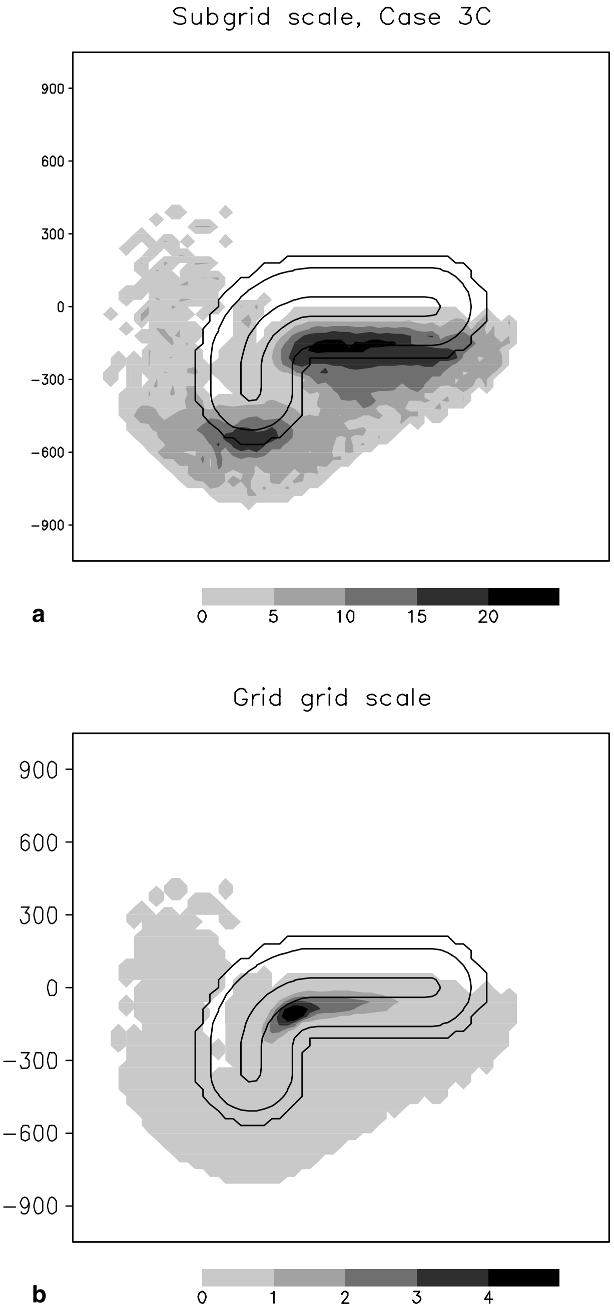

Fig. 14. The accumulated (**a**) unresolved and (**b**) resolvable rainfall (in *mm*) at $Ut/a = 4.32$ for Cases 3C

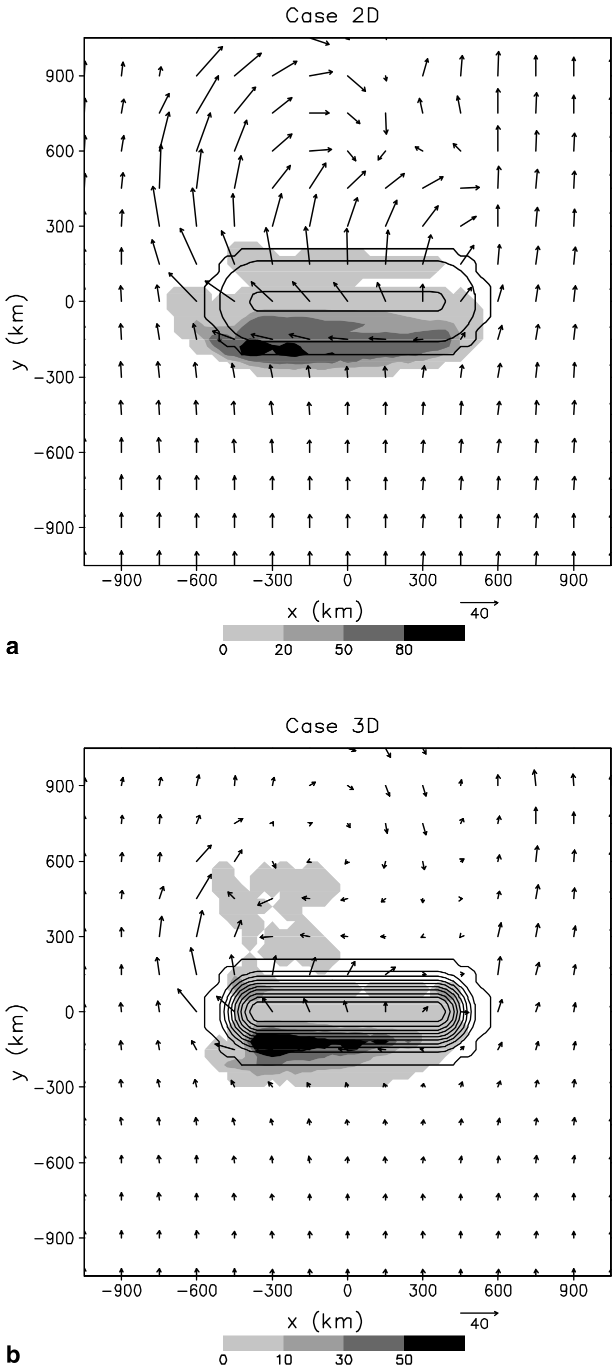

Fig. 15. The surface accumulated rainfall (shaded; in *mm*) and horizontal wind vectors at the first half sigma level at $Ut/a = 17.28$ for (**a**) Case 2D ($U = 15\,ms^{-1}$; $CAPE = 1000\,J\,kg^{-1}$), and (**b**) Case 3D ($U = 7.5\,ms^{-1}$; $CAPE = 1000\,J\,kg^{-1}$)

Figure 15a shows the rainfall and wind vectors for Case 2D with $U = 15\,ms^{-1}$ and CAPE $= 1000\,J\,kg^{-1}$, which is half of the control run in Case 2. In general, the flow responses are similar to Case 2, except that the upstream convective system and simulated rainfall in the present case are confined near the foothills and upwind slope compared to those in Case 2 (Fig. 3c). In other words, the upstream convective system becomes more stationary, though the flow response still belongs to Regime II. To illustrate this further, we may compare the rainfall patterns in Cases 3 (Fig. 6a and b) and 3D (Fig. 15b). It appears that the upstream flow becomes quasi-stationary, which is similar to that in Regime II. Thus, we may conclude that the upstream flow tends to shift to a higher regime when the CAPE is reduced. In general, the strength of the convective system decreases when the CAPE decreases, and the induced surface cold pool becomes weaker. Therefore, the strength of the cold pool against the convective system to propagate downstream is weaker. In other word, the system is easier to move downstream when the CAPE is reduced, and the flow tends to transit to a higher regime. Note that the moist Froude number slightly decreases when the CAPE decreases, and the Froude number cannot be used to define a flow regime directly when different CAPEs are considered. Therefore, a two-dimensional parameter relationship might be required. This is beyond the scope of this study, and we will pursue it in future studies.

4. Concluding remarks

Based on idealized numerical simulations using the Weather and Research Forecast (WRF) model, at least three flow regimes are identified for a conditionally unstable, rotational, horizontally homogeneous, uniformly stratified flow over an idealized, three-dimensional mesoscale mountain stretched spanwise to the impinging flow: (I) a quasi-stationary upslope convective system and an upstream-propagating convective system, (II) a quasi-stationary upslope convective system, and (III) a stationary upslope convective system and a quasi-stationary downstream convective system. The major differences from a similar type of flow, but with no rotation, over a two-dimensional (2-D) mountain range (Chu and Lin, 2000) are: (1) the flow is allowed to go around the mountain, which helps produce outward-moving convective lines upstream of the mountain, and to curve into the mountain on the lee side, (2) a relatively large amount of rainfall can be produced over upwind slopes, instead of at the mountain peak, under the presence of a strong wind speed (e.g., $U = 15\,ms^{-1}$ in regime II and $U = 30\,ms^{-1}$ in regime III), which is more consistent with observations, (3) in regime I, besides an upstream propagating convective system as that in the 2D simulation, a quasi-stationary upslope convective system is identified, and (4) in regime III, a quasi-stationary downstream convective system instead of a downstream propagating convective system (2D) is obtained. A very heavy upslope rain is produced in regime III, due to the strong orographic lifting.

Similar to the dry flow, the moist flow passes anticyclonically over the mountain ridge and produces a high-low couplet of pressure perturbation, which is oriented in the southwest–northeast direction due to the rotational effect. The moist flow is deflected slightly eastward (to the right) upstream of the low-level MCS convergence zone. The Coriolis force, by deflecting the incipient southerly flow and producing an east–southeasterly barrier wind, allows a portion of the incoming upstream flow to make a transition from ‘‘flow-around’’ the eastern upslope to ‘‘flow-over’’ the western upslope. These barrier winds induce stronger upward motion over the southwestern slope of the mountain ridge and consequently produce heavier rainfall over that region. In fact, we found that the Coriolis force helps produce heavy upslope rainfall because a more stationary system is developed.

We have also investigated the effects of concave mountain geometry on orographic precipitation by adopting an arc-shaped mountain. In this study, we found that the addition of the western flank of the arc-shaped mountain reduces the southeasterly barrier wind which makes the maximum rainfall move towards east of the windward slope. A lower Froude number flow, such as $F_w = 0.333$, is able to produce the maximum rainfall close to the concave region. In addition, we found that the upward vertical motion is not produced by the convergence between the Coriolis force-deflected southeasterly jet and southwesterly flow along the eastern edge of the western flank. However, this type of flow situation may occur in the real atmosphere since heavy rainfall is often associated with a LLJ advancing rapidly in conjunction with a deep trough moving eastward.

Several other important facts can also be found in this study. The ratio of the maximum grid-scale rainfall to the subgrid-scale rainfall increases when the moist Froude number increases. When the spatial resolution increases, more grid-scale rainfall will be expected, and more rainfall might be potentially produced near the concave region corresponding to the vertical velocity there. When the CAPE decreases, it is found that the upstream moist flow tends to shift to a higher flow regime. Therefore, the Froude number cannot be used to define a moist flow regime solely when different CAPEs are considered. In another word, other parameters (such as CAPE) might play an important role in determining moist flow regimes, and this will be studied in the future.

Acknowledgments

This work is supported by US NSF Grant ATM-0096876. The authors would like to acknowledge the WRF model development team for their efforts in developing this model. Further thanks are given to S. Chiao, J. A. Thurman, Dr. K. D. Pfeiffer, and Dr. J. J. Charney for their help. Discussion with Drs. J. Dudhia and M. L. Kaplan is appreciated. Special thanks are given to Dr. R. P. Weglarz at Western Connecticut State University for proofreading, technical editing, and offering valuable, constructive comments on the manuscript. The computations were performed on NCAR supercomputers.

References

Banta RM (1990) The role of mountain flows in making clouds. In: Atmospheric processes over complex terrain (Blumen W, ed). Meteor Monogr, pp 229–282

Bauer MH, Mayr GJ, Vergeiner I, Pichler H (2000) Strongly nonlinear flow over and around a three-dimensional mountain as a function of the horizontal aspect ratio. J Atmos Sci 57: 3971–3991

Binder P, Schär C (eds) (1996) MAP design proposal. MeteoSwiss, 75 pp (Available from the MAP Programme Office, MeteoSwiss, 8044 Zurich, Switzerland)

Buzzi A, Foschini L (2000) Mesoscale meteorological features associated with heavy precipitation in the southern Alpine region. Meteorol Atmos Phys 72: 131–146

Chen S-H, Dudhia J (2000) Annual report: WRF physics (Available at http://wrf-model.org)

Chen S-H, Sun W-Y (2002) A one-dimensional time-dependent cloud model. J Meteor Soc Japan 80: 99–118

Chen SS, Frank WM (1993) A numerical study of the genesis of extratropical convective mesovortices. Part I: Evolution and dynamics. J Atmos Sci 50: 2401–2426

Chen Y-L, Li J (1995) Characteristics of surface pressure and wind patterns over the island of Taiwan during TAMEX. Mon Wea Rev 123: 691–716

Chiao S, Lin Y-L (2003) Numerical modeling of an orographically enhanced precipitation event associated with tropical storm Rachel over Taiwan. Wea Forecast 18: 325–344

Chu C-M, Lin Y-L (2000) Effects of orography on the generation and propagation of mesoscale convective systems in a two-dimensional conditionally unstable flow. J Atmos Sci 57: 3817–3837

Dyer AJ, Hicks BB (1970) Flux-gradient relationships in the constant flux layer. Quart J Roy Meteor Soc 96: 715–721

Emanuel KA (1994) Atmospheric convection. Oxford University Press, 580 pp

Hong S-Y, Pan H-L (1996) Nonlocal boundary layer vertical diffusion in a medium-range forecast model. Mon Wea Rev 124: 2322–2339

Houze RA Jr (1993) Cloud dynamics. Academic Press. 573 pp

Kain JS, Fritsch JM (1993) Convective parameterization for mesoscale models: The Kain-Fritsch scheme. Meteor Monogr, Amer Meteor Soc 46: 165–170

Klemp JB, Wilhelmson R (1978) The simulation of three-dimensional convective storm dynamics. J Atmos Sci 35: 1070–1096

Li J, Chen Y-L, Lee W-C (1997) Analysis of a heavy rainfall event during TAMEX. Mon Wea Rev 125: 1060–1082

Lin Y-L (1993) Orographic effects on airflow and mesoscale weather systems over Taiwan. Terr Atmos Ocean 4: 381–420 (Available from the corresponding author)

Lin Y-L, Farley RD, Orville HD (1983) Bulk parameterization of the snow field in a cloud model. J Clim Appl Meteor 22: 40–63

Lin Y-L, Lin N-H, Weglarz RP (1992) Numerical modeling studies of lee mesolows, mesovortices, and mesocyclones with application to the formation of Taiwan mesolows. Meteorol Atmos Phys 49: 43–67

Lin Y-L, Chiao S, Wang T-A, Kaplan ML, Weglarz RP (2001) Some common ingredients for heavy orographic rainfall. Wea Forecast 16: 633–660

Michalakes J, Chen S-H, Dudhia J, Hart L, Klemp J, Middlecoff J, Skamarock W (2001) Development of a next generation regional weather research and forecast model. In: Developments in teracomputing. Proc 9th ECMWF Workshop on the Use of High Performance Computing in Meteorology (Zwieflhofer W and Kreitz N, eds). Singapore: World Scientific Publishing, pp 269–276

Miglietta MM, Buzzi A (2001) A numerical study of moist stratified flows over isolated topography. Tellus 53A: 481–499

Olafsson H, Bougeault P (1997) The effect of rotation and surface friction on orographic drag. J Atmos Sci 54: 193–210

Paulson CA (1970) The mathematical representation of wind speed and temperature profiles in the unstable atmospheric surface layer. J Appl Meteor 9: 857–861

Pierrehumbert RT, Wyman B (1985) Upstream effects of mesoscale mountains. J Atmos Sci 42: 977–1002

Queney P (1948) The problem of airflow over mountains: A summary of theoretical studies. Bull Amer Meteor Soc 29: 16–26

Raymond R, Rotunno R (1989) Response of a stably stratified flow to cooling. J Atmos Sci 46: 2830–2837

Rotunno R, Ferretti R (2001) Mechanisms of intense Alpine rainfall. J Atmos Sci 58: 1732–1749

Rutledge SA, Hobbs PV (1984) The mesoscale and microscale structure and organization of clouds and precipitation in midlatitude cyclones. XII: A diagnostic modeling study of precipitation development in narrow cloud-frontal rainbands. J Atmos Sci 20: 2949–2972

Schneidereit M, Schär C (2000) Idealised numerical experiments of Alpine flow regimes and southside precipitation events. Meteorol Atmos Phys 72: 233–250

Skamarock WC, Klemp JB, Dudhia J (2001) Prototypes for the WRF (Weather Research and Forecast) model. 9th Conf Meso Processes, AMS, J11–J15 (see also http://www.wrf-model.org)

Smith RB (1979) The influence of mountains on the atmosphere. Adv Geophys 21 (Saltzman B, ed). Academic Press, pp 87–230

Smith RB (1980) Linear theory of stratified hydrostatic flow past an isolated mountain. Tellus 32: 348–364

Smith RB, Gronas A (1993) Stagnation points and bifurcation in 3-D mountain airflow. Tellus 45A: 28–43

Smolarkiewicz PK, Rotunno R (1989) Low Froude number flow past three-dimensional obstacles. Part I: Baroclinic generated lee vortices. J Atmos Sci 46: 1154–1164

Smolarkiewicz PK, Rasmussen RM, Clark TL (1988) On the dynamics of Hawaiian cloud bands: Island forcing. J Atmos Sci 45: 1872–1905

Stein J (2001) Numerical exploration of dry and moist airflow regimes over idealized Alps. MAP Newsletter, No. 15, pp 272–275 (Available from the website: http://www.map.ethz.ch/newsletter15.htm)

Sun W-Y, Chern JD, Wu C-C, Hsu W-R (1991) Numerical simulation of mesoscale circulation in Taiwan and surrounding area. Mon Wea Rev 119: 2558–2573

Thorsteinsson S, Sigurdsson S (1996) Orogenic blocking and deflection of stratified air flow on an f-plane. Tellus 48A: 572–583

Trub J, Davies HC (1995) Flow over a mesoscale ridge: pathways to regime transition. Tellus 47A: 502–524

Corresponding author's address: Dr. Shu-Hua Chen, Department of Land, Air, and Water Resources, University of California, Davis, CA 95616-8627, USA (E-mail: shachen@ucdavis.edu)